Understand and correct for the low wind effect on the SPHERE and GRAVITY+ adaptive optics

Nicolas Pourré, Jean-Baptiste Le Bouquin, Julien Milli, Jean-François Sauvage, Thierry Fusco, Carlos Correia, Sylvain Oberti

To cite this version:

Nicolas Pourré, Jean-Baptiste Le Bouquin, Julien Milli, Jean-François Sauvage, Thierry Fusco, et al.. Understand and correct for the low wind effect on the SPHERE and GRAVITY+ adaptive optics. SPIE Astronomical Telescopes + Instrumentation, Jul 2022, Montréal, Canada. pp.201, 10.1117/12.2629793 . hal-03940875

HAL Id: hal-03940875
https://hal.science/hal-03940875v1

Submitted on 25 Jan 2023

Understand and correct for the low wind effect on the SPHERE and GRAVITY+ adaptive optics

Nicolas Pourré[a], Jean Baptiste Le Bouquin[a], Julien Milli[a], Jean-François Sauvage[b,c], Thierry Fusco[b,c], Carlos Correia[d], and Sylvain Oberti[e]

[a]Univ. Grenoble Alpes, CNRS, IPAG, 38000 Grenoble, France
[b]DOTA, ONERA, Université Paris Saclay (COmUE), France
[c]Aix Marseille Univ, CNRS, CNES, LAM, Laboratoire d'Astrophysique de Marseille, Marseille, France
[d]Space ODT - Optical Deblurring Technologies, Rua Direita de Francos, 1021, Rés-Do-Chão Esquerdo 4250-194 Porto, Portugal
[e]European Southern Observatory, Karl-Schwarzschild-Straße 2, 85748 Garching, Germany

ABSTRACT

The low wind effect is responsible for uncorrected aberrations that reduce the contrast of exoplanet observations during the nights where the atmospheric conditions are the best. This effect arises at the aperture of 8 meter telescopes such as the Very Large Telescope (on SPHERE, Adaptive Oprics Facility (AOF)), Subaru (on SCExAO) and Gemini South (GPI). It is a thermal effect occuring at the spiders that hold the secondary mirror. We use numerical simulations to understand why the high-order adaptive optics fail to correct for low wind effect. Our simulations show that the adaptive optics might amplify/create most of the undesired residuals. We propose a mitigation strategy based on both Shack-Hartmann measurements and H-band focal plane images. We speculate that, contrary to a common belief, the low wind effect could be a local effect on the pupil that is spread out by the adaptive optics loop.

Keywords: low wind effect, high-contrast, adaptive optics

1. INTRODUCTION

The goal of obtaining direct images of exoplanets orbiting their host star has driven tremendous efforts in designing instruments. Instruments tended toward high order extreme Adaptive Optics to bring the biggest existing telescopes to their diffraction limit. On the way, numerous obstacles appeared such as the vibrations and the non-common-path aberrations. Additionally, in this race for high angular resolution and high contrast, an unexpected hurdle has became of prime concern: the low wind effect (LWE). It have been first detected during the commissioning of the Spectro-Polarimetic High contrast imager for Exoplanets REsearch (SPHERE) at the Very Large Telescope (VLT)[1] and has been considered as the main limitation of the instrument at that time.[2]

The LWE have first been detected because of its strong impact on focal plane images. When the effect is present, near-infrared images display bright lobes at the location of the first Airy ring and even a fragmentation of the core of the point-spread-function in the strongest cases. On SPHERE, these secondary lobes are responsible for starlight leaking through the coronagraphs and degrade the raw contrast by a factor 50 at 100 mas.[3] Also, the degradation of the point-spread-function prevents non-coronagraphic exoplanets direct observations at short angular separation. The bright lobes location and intensity vary in a timescale between 1 and 2 seconds on the VLT but the analysis of longer image sequence show that part of the effect is consistent over around one minute. To further investigate the LWE, measurements have been performed on SPHERE with the Zernike phase mask ZELDA[4,5] . It allows for a conversion of pupil phase aberrations into intensity on the image plane (Fig. 2). The ZELDA measurements during LWE events revealed sharp optical path difference (OPD) discontinuities at the spiders and piston, tip, tilt aberrations restricted to the four pupil quadrants.

Send correspondence to Nicolas Pourré
E-mail: nicolas.pourre@univ-grenoble-alpes.fr

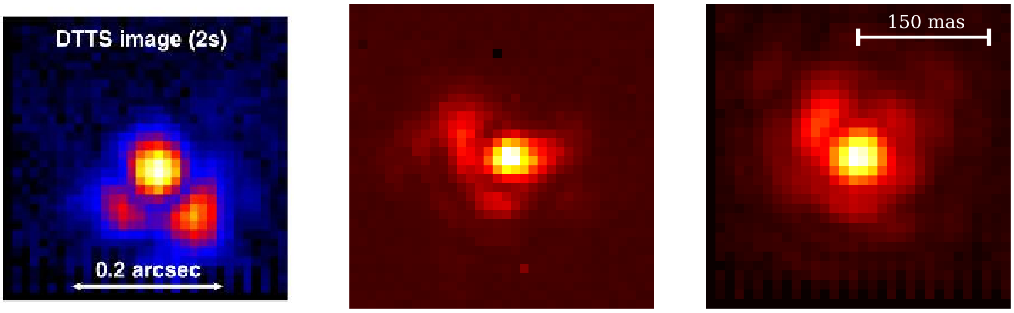

(a) (b) (c)

Figure 1: Three LWE point spread functions averaged over different durations. (a) Image from the Differential Tip Tilt Sensor (DTTS) on SPHERE taken from Milli et al. 2018. The image is at H-band and is averaged over 2 seconds. (b) Image with IRLOS at H-band from the AOF. Averaged over 10 seconds. (c) Image from the DTTS, average over 1.5 minute.

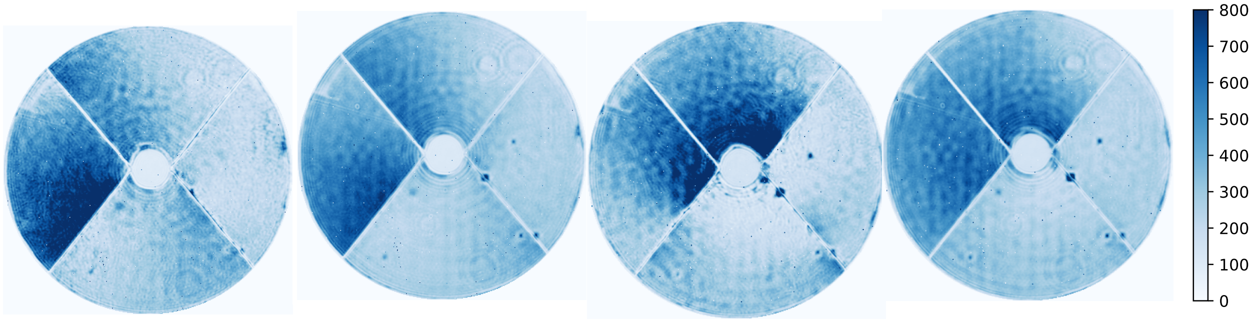

(a) 1 s DIT at 1:52 UT (b) 2 min average at 1:52 UT (c) 1 s DIT at 2:44 UT (d) 2 min average at 2:44 UT

Figure 2: Pupil OPD measurement with the Zernike phase mask ZELDA on SPHERE. Taken during the LWE night of 8 October 2014 during SPHERE commissioning.

The low wind effect appears during the nights with surface wind below 4 m .s^{-1}.[3] In this condition, the air is not well mixed at the telescope aperture and a laminar air flow can develop around the spiders holding the secondary mirror. The air cools down at the contact of the spiders and this thermal exchange is responsible for layers of colder air (and lower optical index) in the telescope pupil, creating aberrations with sharp OPD discontinuities. The LWE is present during the nights where otherwise the atmospheric conditions are the best, therefore this effect has to be mitigated. There has been efforts in various directions to correct for LWE. First of all, at the VLT a coating has been applied on the spiders of the Unit Telescopes 3 to limit emissivity in the mid-infrared. This passive solution limited the occurrence of the phenomenon from 20% to 3.5% of the observing time.[3] There are also mitigation strategies relying on a focal plane measurement of the LWE aberrations and a correction by the adaptive optics (see Vievard et al. 2019[6] for an overview). Some of these active techniques have already been tested in laboratory and on-sky (e.g. Fast & Furious algorithm[7,8]).

Here we investigate the effect of the LWE phase discontinuities on a Shack-Hartmann based adaptive optics. This investigation will bring an explanation for the post-AO residuals observed on SPHERE during LWE events. Also we will propose an active mitigation strategy that uses the SH measurements and a focal plane analysis. This mitigation algorithm can be implemented on any instrument with a high-resolution SH and affected by the LWE such as SPHERE and GRAVITY+ at the VLT. In the paper, non-bold variables are scalars, bold variables are vectors and bold-underlined variables are matrices. $\cdot$ is for matrix product.

2. SHACK-HARTMANN MEASUREMENT OF DISCONTINUITIES

The most striking feature of the LWE aberrations measured by the ZELDA sensor is the sharp OPD discontinuities. We will investigate how discontinuities are measured by the SH wavefront sensor. For this, we will use numerical simulations at the SH sub-aperture scale and study the sensitivity to phase discontinuities. We will stay in the SPHERE and GRAVITY+ configuration with spiders obstructing 25% of the SH sub-aperture and with a sub-aperture field of view of 3.5 λ/d, with d the width of the sub-apertures. The focal plane is oversampled compared to the realistic 6x6 pixels per spot.

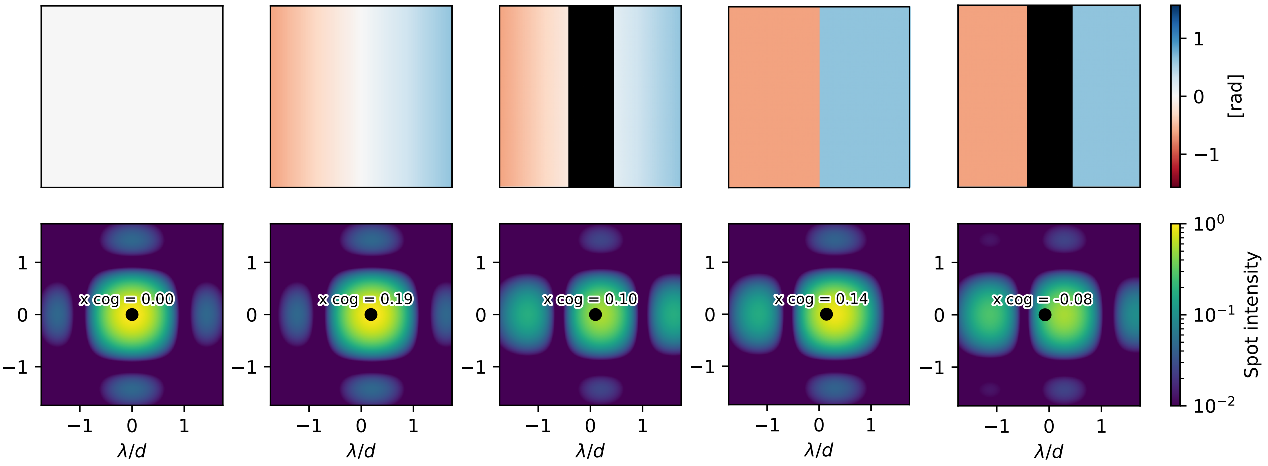

(a) (b) (c) (d) (e)

Figure 3: Square aperture phase (top) and corresponding SH spot (bottom) in different configurations. (a) no aberration. (b) phase slope of $0.2 \times 2\pi$ amplitude. (c) phase slope obstructed by a spider. (d) phase discontinuity with same peak-to-valley amplitude as the slope. (e) phase discontinuity obstructed by a spider. The black dot displays the center-of-gravity measured in the 3.5 λ/d field of view.

Figure 3 displays how a spot can be distorted by a phase discontinuity across the sub-aperture and how the center-of-gravity of the spot can be affected. A phase slope of amplitude $\Delta\varphi = a \times 2\pi$ rad induces a spot displacement of $a \times \lambda/d$ at the focal plane. In this example $a = 0.2$, so the measurement accuracy is given by the difference between the `x cog` value displayed and 0.2. Regarding morphological features, we can see that the difference between a phase slope and a phase discontinuity (Fig. 3b and 3d) is that the discontinuity is responsible for a bright secondary lobe. For this reason, the center-of-gravity in the restricted field of view do not measure the right value (on a infinite field of view it would measure 0.2 λ/d, the right value for the phase step introduced). This phenomenon is even more prominent when the discontinuity is obstructed by a spider (Fig. 3c and 3e). In this case the sub-aperture sensitivity to the phase discontinuity is reduced and can even be reversed.

A more detailed study of the sub-aperture sensitivity to a phase discontinuity at different positions is displayed on Fig. 4. It shows that the sensitivity is different depending on the discontinuity location in the sub-aperture. We recover an expected result, if the discontinuity is located at the border of the sub-aperture the ability of the sub-aperture to measure the phase step is dramatically reduced. For a non-obstructed discontinuity the sensitivity varies by up to 20% depending on the location of the discontinuity. For a discontinuity obstructed by a spider, the measurement never gets close to the expected value a, leading to a greatly erroneous estimation of the phase step amplitude.

The erroneous measurement by the SH does not come from the wrapping for phase discontinuities with amplitudes higher than $\lambda/4$. Figure 5 shows that even in the weak phase regime the sub-aperture sensitivity to the phase step depends on the position of the step. As expected, this bad sensitivity is even worse when the discontinuity is obstructed by a spider. Here the sensitivity is reversed even in the weak-phase regime. Overall, it demonstrates the inability of the center of gravity to measure obstructed phase discontinuities on a restricted field of view. Unfortunately this is precisely the kind of aberrations the LWE induces.

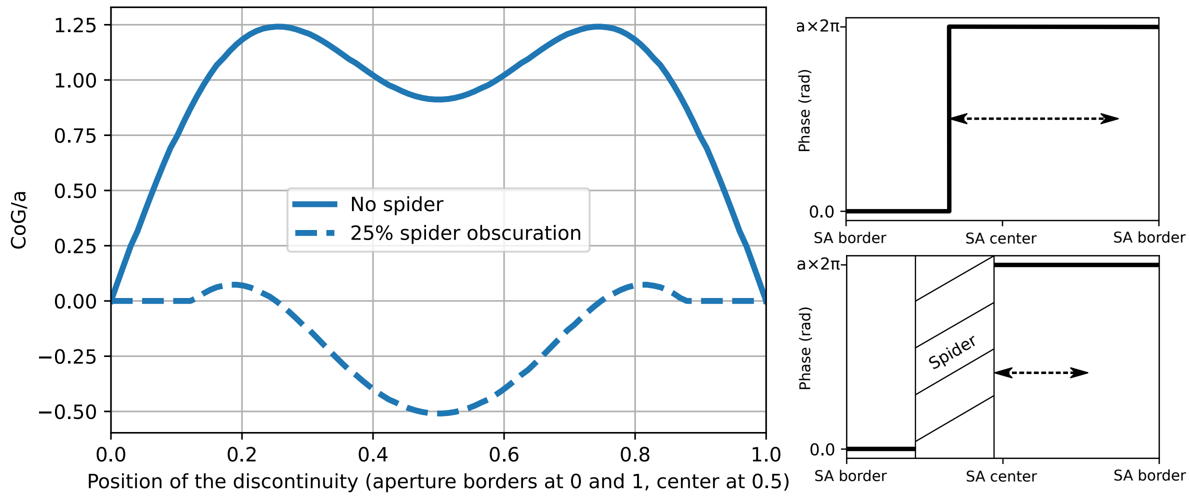

(a) (b)

Figure 4: (a) Center-of-gravity (CoG) with respect to the position of the discontinuity in the sub-aperture (SA), with and without spider. The center-of-gravity is scaled by the discontinuity amplitude a. $CoG/a = 1$ corresponds to a perfect measurement of the phase step. The simulations are carried out in the weak-phase regime ($a = 0.02$) (b) 1D sketches for the both cases with and without spider.

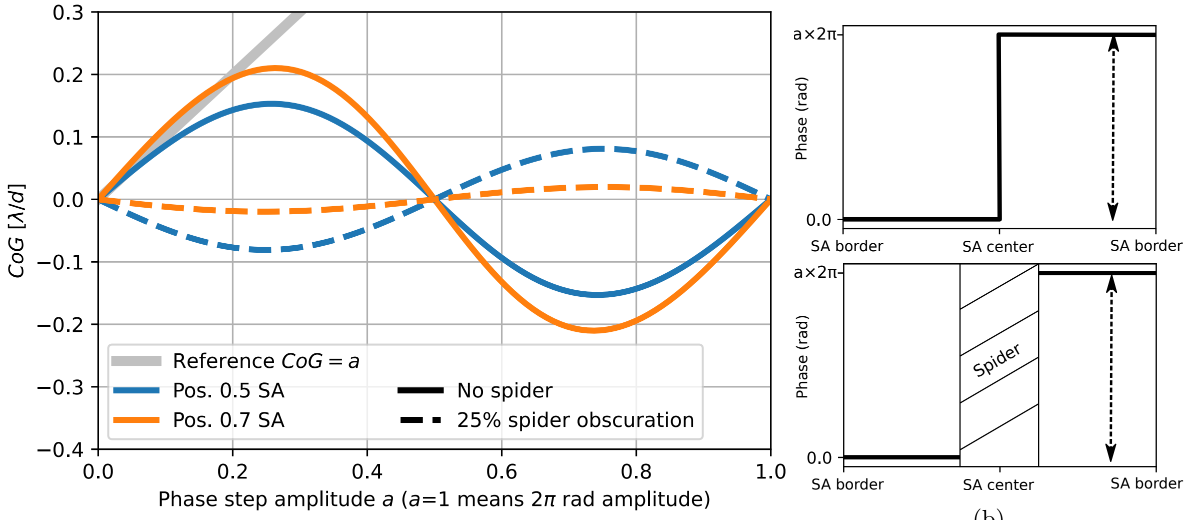

(a) (b)

Figure 5: (a) Center-of-gravity (CoG) with respect to the amplitude of the discontinuity for two positions in the sub-aperture (SA), with and without spider. The grey line shows the ideal measurement for $CoG = a$. (b) 1D sketches for the both cases with and without spider at position 0.5 SA.

3. IMPACT ON THE ADAPTIVE OPTICS

3.1 The uncorrected modes

In this section, we will use an end-to-end simulation with HCIPy[9] to investigate for the post-AO residuals when the pupil phase contains discontinuities at the spiders. The design of the AO simulation is close to the SPHERE and GRAVITY+ design with a deformable mirror (DM) of 1377 actuators (41 actuators in a pupil diameter) controlled by the firsts 990 Karhunen-Loève (KL) modes. The wavefront sensor is a 40x40 SH at $\lambda = 700$ nm and each sub-aperture spot is sampled by 6x6 pixels. For now we use no spatial filter and no spot weighting. We exclude sub-apertures that receive less than 50% of the nominal flux but always keep sub-apertures located behind the spiders. Only sub apertures located behind (or too close) to the secondary mirror central obscuration or the pupil border are excluded. The pupil is the VLT Unit Telescopes pupil with a 8 m diameter, 1.1 m central obscuration and four spiders of 5 cm width.

To simulate LWE, we will inject aberrations at the pupil-plane in the shape of pistons restricted to the four pupil quadrants separated by the spiders (petal-pistons thereafter called PP) and tip-tilts restricted to the four pupil quadrants (petal-tip-tilts thereafter called PTT). Figure 6 shows that a PP is not corrected by the AO. Even if it stays in the weak-phase regime. The PP do not induce any SH response in the quadrant and is only seen through its impact at the discontinuities obstructed by spiders. The previous section have shown that this measurement is greatly faulty, therefore the PP modes are unseen and uncorrected.

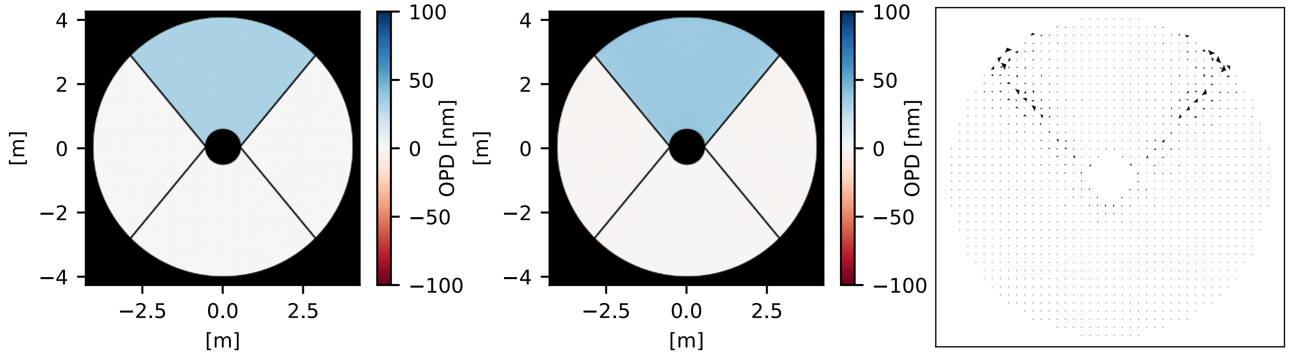

(a) PP perturbation before AO (b) Residuals after AO convergence (c) SH slopes at AO convergence

Figure 6: AO response to a petal-piston of 32 nm peak-to-valley amplitude (weak-phase regime) as perturbation. (a) perturbation before AO, the OPD is 21 nm rms. (b) post-AO residuals after convergence, the OPD rms is 24 nm rms. (c) SH slopes at convergence.

Figure 7 shows that the AO loop behaviour is different when the perturbation is a PTT. Here again, the SH response to the perturbation at the discontinuities is faulty but the SH is sensitive to the tip-tilt inside the quadrant that is a constant phase slope. When we close the loop, the AO converges to a state where neither the slopes nor the OPD is equal to zero. Rather, we see that the residual slopes pattern is composed of a global curl around the central obscuration and of local curl on the top-right spider.

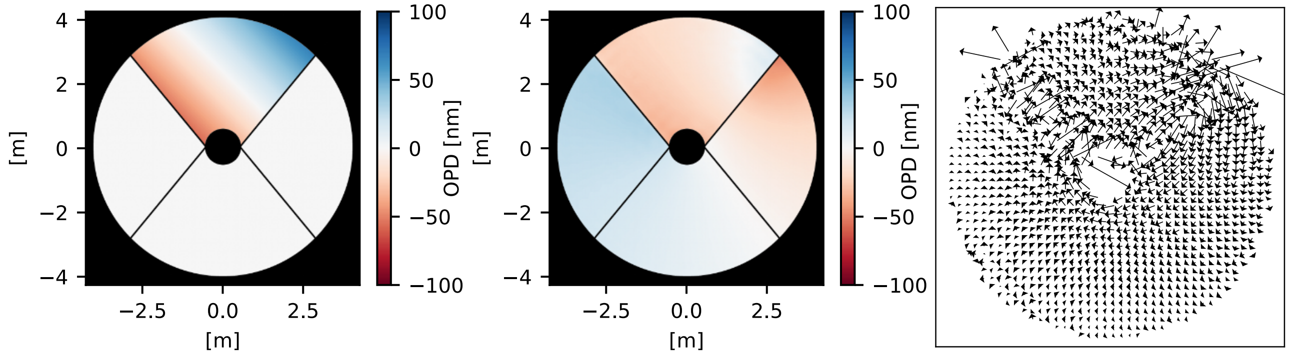

(a) PTT perturbation before AO (b) Residuals after AO convergence (c) SH slopes at AO convergence

Figure 7: AO response to a petal-tip-tilt of 100 nm peak-to-valley amplitude (weak-phase regime) as perturbation. (a) perturbation before AO, the OPD is 16 nm rms. (b) post-AO residuals after convergence, the OPD rms is 19 nm rms. (c) SH slopes at convergence.

There is a fundamental reason for these residuals. A well known vector operators law states that:

$$\overrightarrow{curl}\;\overrightarrow{grad}\;\mathscr{S} = 0 \tag{1}$$

with $\mathscr{S}$ a continuous surface. In our AO system, the $\mathscr{S}$ is the DM surface and the $\overrightarrow{grad}$ operator is the SH. Then we understand that the DM cannot induce a curl in the SH slopes. The other way around, a curl in the

SH slopes do not projects on the Karhune-Loève basis (or any other DM subspace) and remains uncorrected. This statement is true for any curl structure, be it global (at the pupil scale) or local (around a spider). Then, the question arises: why this curl structure appeared in our SH slopes if the DM cannot create it? The Figure 8 helps to understand the process. A perfect wavefront sensor (Fig. 8b) would measure the right amplitude for the discontinuity. Over a closed path, the phase step amplitude would compensates for the slope induced by the rest of the pupil and the resulting slope map would not contain any curl. The SH is not this perfect sensor, we have shown in the previous section that the SH has a reduced sensitivity to phase discontinuities. It will make a good measurement of the phase slopes on the pupil but will underestimate the phase discontinuities amplitude (Fig. 8c). For this reason the SH slopes will contain a curl component that will remain uncorrected even after the AO loop convergence. Interestingly, through this process a perturbation initially restricted to one quadrant can spread over the whole pupil after the AO convergence.

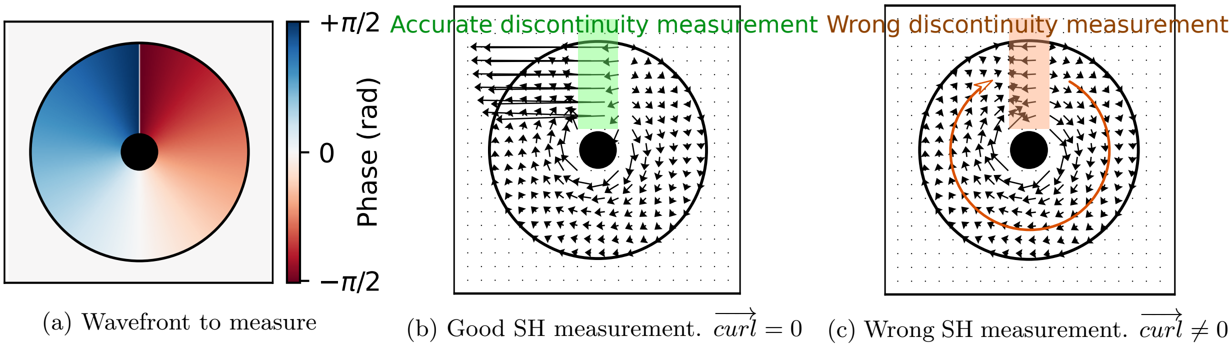

(a) Wavefront to measure (b) Good SH measurement. $\overrightarrow{curl} = 0$ (c) Wrong SH measurement. $\overrightarrow{curl} \neq 0$

Figure 8: Explanation for how a curl structure can arise in the slopes from a bad discontinuity measurement.

With the explanations for the badly corrected PP and PTT we can now reproduce the post-AO residuals observed with the ZELDA sensor on SPHERE during LWE nights. To achieve this, we refine the AO to make it closer to the SPHERE AO. We included a spatial filter of 2 λ/d, d being the width of one SH subaperture. We also included a Gaussian weighting of the SH spots for the center of gravity calculations. Finally, we included the Differential Tip-Tilt Sensor (DTTS) of the instrument.[10] In SPHERE, the goal of this sub-system is to ensure the centering of the central star behind the coronagraph. It measures the residual tip-tilt thanks to a centre of gravity measurement on a dedicated H-band camera and send a corrective command to a specific tip-tilt mirror before the SH. In our simulations the DTTS appeared to be responsible for residual tip-tilts when the system is exposed to a LWE perturbation. It is expected since we have shown that phase discontinuities can mislead a center of gravity mesurement on a spot. With this improved AO simulation, we are able to reproduce qualitatively the post-AO residuals observed on SPHERE (Fig. 9).

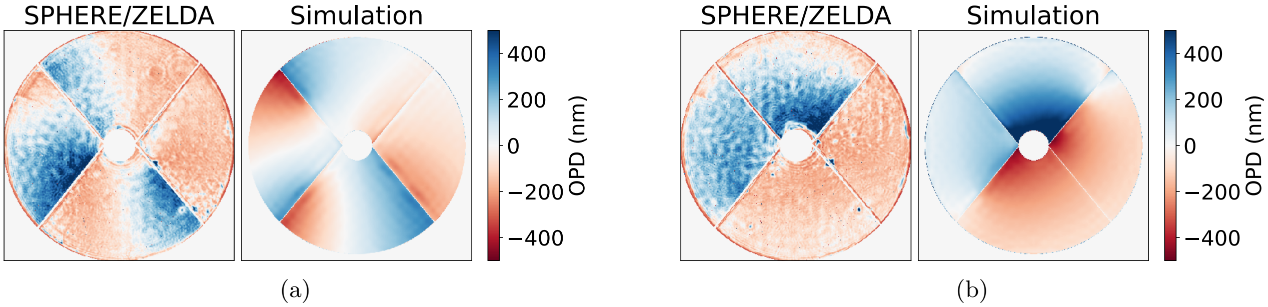

(a) (b)

Figure 9: Qualitative reproduction of the LWE post-AO residuals observed on SPHERE with the ZELDA sensor.

3.2 Local perturbations

So far, we have simulated LWE with petal-pistons and petal-tip-tilts perturbations at the pupil plane. However, it would be surprising if the cooling of the spiders on the ambient air was creating regular pistons or tip-tilt on a whole pupil quadrant. We would expect the colder layer to be localized along the spiders and have a limited spatial extension. We ran simulations with perturbations composed of OPD gradients along the spiders rather than full quadrant PP and PTT (Fig. 10). We have shown in our analysis that the bad correction of LWE aberrations come from an erroneous measurement of discontinuities by the SH. Our simulations with a local OPD gradient confirms that a discontinuity is enough to create all the post-AO residuals observed on SPHERE. If the sum of all OPD gradient along the spiders contribute in the same rotation direction there will be a curl pattern in the residual SH slopes and a vortex pattern in the phase. Two OPD gradients contributing in an opposite direction will induce petal-pistons in the vortex phase. These simulations show that the AO can be responsible for creating most of the residual aberrations that degrade focal plane images during LWE events. It contradicts the observations of the DM voltages on SPHERE[2] that show no sign of the DM creating the petal aberrations. More work is required to settle this discrepancy.

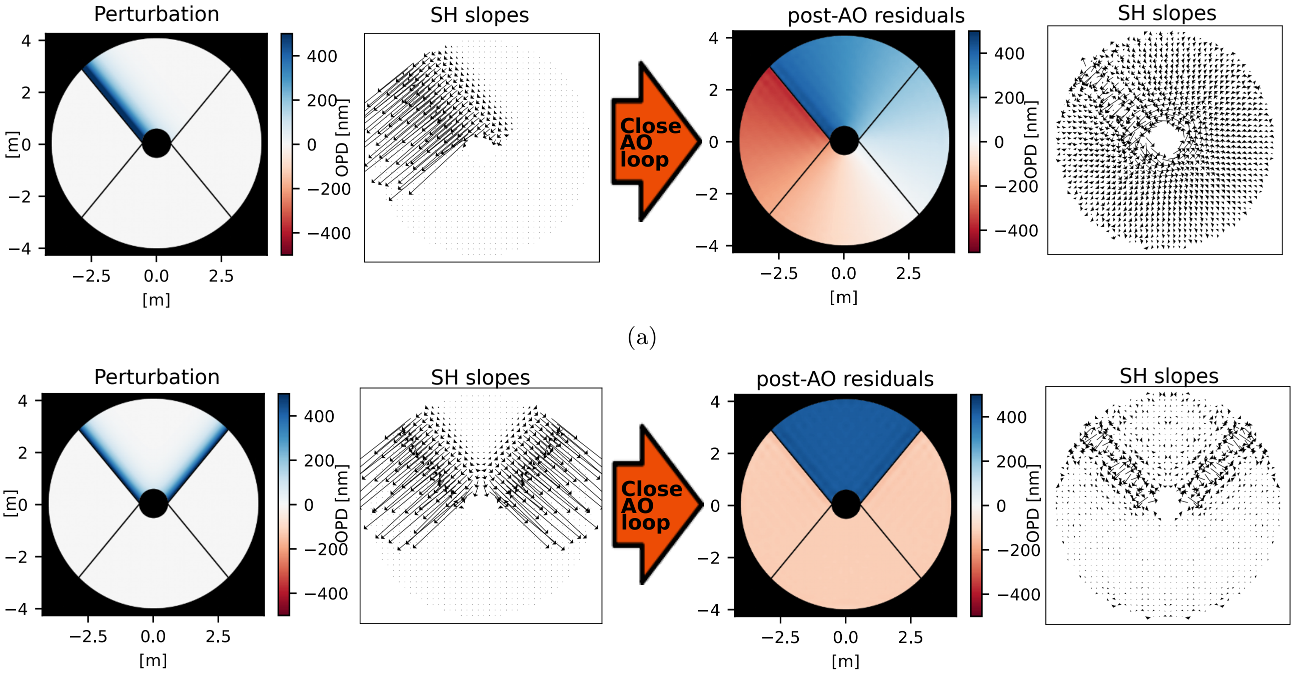

(a)

(b)

Figure 10: Closing the AO loop on OPD gradients along the spiders. (a) one OPD gradient along a spider. The perturbation is of 89 nm rms (Strehl H-band 92%). After AO convergence the residuals are of 225 nm rms (Strehl H-band 69%). (b) two OPD gradients along two different spiders. The perturbation is of 81 nm rms (Strehl H-band 92%). After AO convergence the residuals are of 243 nm rms (Strehl H-band 63%).

3.3 What can we expect on the next generation telescopes?

Next generation giant telescopes (e.g. ELT) have thicker spiders. If the spiders are thicker than the SH subapertures, the wavefront sensor cannot ensure continuity between the separated parts of the pupil and uncorrected petal-pistons appear, this is called the island-effect. In this context there is no phase discontinuity problem since no sub-aperture see two quadrants at the same time but petal-pistons are undetectable by the SH. How does a LWE perturbation is treated by the AO for this kind of pupil?

We ran simulations with SPHERE's AO configuration (1377 actuators, 40x40 SH) but without spatial filter and without weighting of SH spots. To mimic the ELT case, we use the VLT UT pupil but with spiders 40 cm thick. Our study shows that petal-tip-tilts never occur in the post-AO residuals in such a configuration, no matter if we simulate LWE with PP and PTT in the pupil phase or with OPD gradients localized along the spiders (Sect. 3.2). It was expected since PTT come from uncorrected curl structures in the slopes that arise when the SH make a bad measurement of a discontinuity across a sub-aperture. Here no sub-apertures are affected by discontinuities, and so no PTT are visible.

Yet, it does not mean that the LWE perturbation is corrected by the AO. Even worse, the adaptive optics converges to strong PP that are responsible for a degradation of the residual OPD (Fig. 11). Still, these simulations show that in this large spiders configuration the LWE becomes PP problem only.

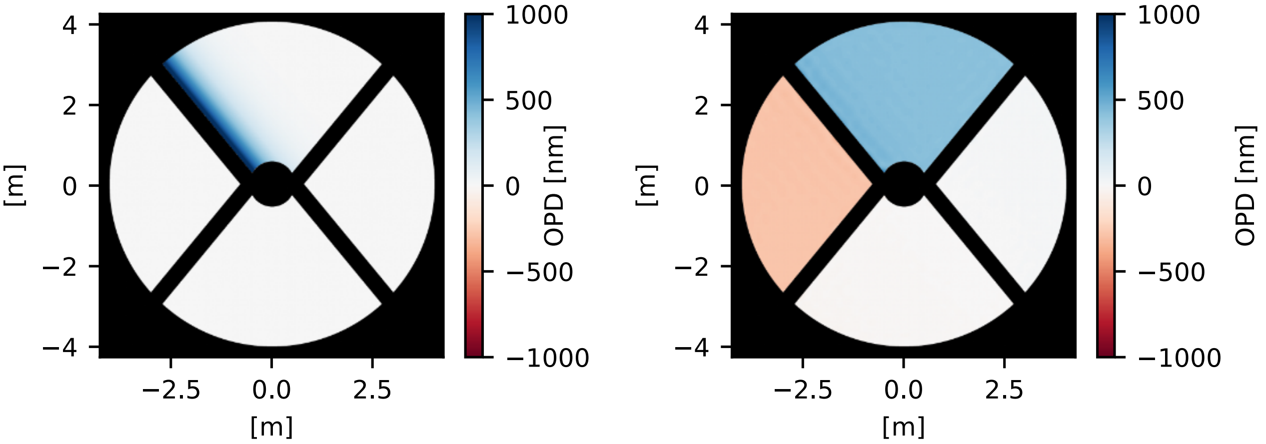

(a) Before AO (b) After AO convergence

Figure 11: (a) Perturbation at the pupil plane composed of an OPD gradient along the top-left spider. The OPD is 150 nm rms. (b) Residuals after AO convergence. The OPD is 255 nm rms.

4. MITIGATION STRATEGY

We describe here a mitigation strategy that uses the SH to measure the PTT modes and a focal plane analysis to measures the PP modes. LWE mitigation algorithms usually control 11 modes (3 petal-pistons and 8 petal-tip-tilt).[8,11,12] Excluding the control of the global piston reduces the number of PP modes to three. Here we propose to use a modified basis where we rearranged the PP and PTT modes into odd and even modes (Fig. 12). Thanks to this new basis, we see that two PTT modes do not contain discontinuities (modes #4 and #8), they are naturally corrected by the AO. Only 9 modes leave to correct, 3 PP modes and 6 PTT modes.

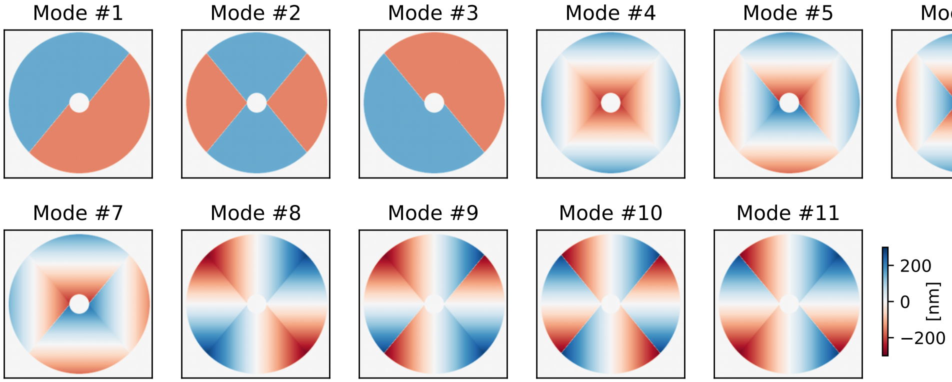

Figure 12: The basis of 11 PP and PTT modes. Odd numbers correspond to odd modes and even numbers correspond to even modes.

For the PTT modes measurement, we propose to use the information in the SH slopes. As we have seen before, the SH is sensitive to the PTT inside the quadrant but poorly sensitive at the discontinuity. Our measurement strategy relies only on the slopes located in the quadrant and discards the slopes located too close to the discontinuity. We select the sub-apertures located in the blue area on Fig. 13 and project the slopes on the 6 PTT modes at each iteration of the AO loop. It gives a measurement at a frequency of 1200 Hz and benefits from the wide SH capture range (PTT up to 2 μm peak-to-valley).

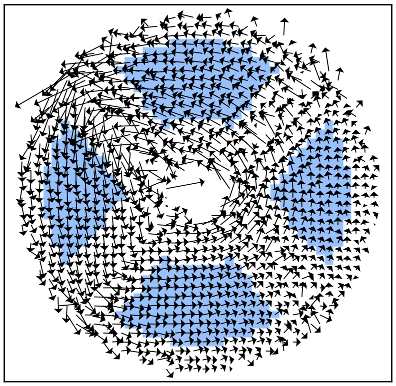

Figure 13: Blue: sub-apertures selected for the PTT measurement.

For a full measurement of the 9 LWE modes, we propose to measure the petal-pistons with a focal plane analysis. The focal plane approach has already been studied extensively for measuring petal modes. It requires a phase diversity or an asymmetric pupil to lift the sign ambiguity on the even modes. But here there are only three PP modes left to measure and, in the basis shown on Fig. 12, we can see that there is only one even PP mode (mode #2). The other two odd PP modes can be measured from a single image as long as the mode amplitude remains in the algorithm capture range (typically OPD peak-to-valley $< \lambda/2$). The method for the PP modes measurement at focal plane is inspired from the Fast & Furious algorithm.[13] In the Fraunhofer approximation the image $\mathbf{I}$ expression is:

$$\mathbf{I} = |\,\mathscr{F}\{\mathbf{A}\exp(i\boldsymbol{\phi})\}\,|^2, \tag{2}$$

with $\mathscr{F}$ the Fourier transform operation, $\mathbf{A}$ the pupil amplitude, $\boldsymbol{\phi}$ the pupil plane phase. If we consider only the three PP modes:

$$\boldsymbol{\phi} = P_1\,\boldsymbol{\phi}_1 + P_2\,\boldsymbol{\phi}_2 + P_3\,\boldsymbol{\phi}_3, \tag{3}$$

with P_1, P_2 and P_3 the modes amplitudes, in the weak-phase regime we can write:

$$\mathbf{I} \approx |\,\mathscr{F}\{\mathbf{A} + i\,P_1\mathbf{A}\boldsymbol{\phi}_1 + i\,P_2\mathbf{A}\boldsymbol{\phi}_2 + i\,P_3\mathbf{A}\boldsymbol{\phi}_3)\}\,|^2. \tag{4}$$

Let us define the following notations:

$$\begin{aligned}
\tilde{\mathbf{A_0}} &= \mathscr{F}\{\mathbf{A}\},\\
\tilde{\mathbf{A_1}} &= \mathrm{Im}\{\,\mathscr{F}\{\mathbf{A}\boldsymbol{\phi}_1\}\,\},\\
\tilde{\mathbf{A_2}} &= \mathscr{F}\{\mathbf{A}\boldsymbol{\phi}_2\},\\
\tilde{\mathbf{A_3}} &= \mathrm{Im}\{\,\mathscr{F}\{\mathbf{A}\boldsymbol{\phi}_3\}\,\}.
\end{aligned}$$

Finally, splitting the image into an odd and an even component we obtain:

$$\mathbf{I}_e \approx \tilde{\mathbf{A_0}}^2 + P_1^2\tilde{\mathbf{A_1}}^2 + P_2^2\tilde{\mathbf{A_2}}^2 + P_3^2\tilde{\mathbf{A_3}}^2 + 2\,P_1\,P_3\,\tilde{\mathbf{A_1}}\,\tilde{\mathbf{A_3}}, \tag{5}$$

$$\mathbf{I}_o \approx -2\,P_1\,\tilde{\mathbf{A_0}}\tilde{\mathbf{A_1}} - 2\,P_3\,\tilde{\mathbf{A_0}}\tilde{\mathbf{A_3}}. \tag{6}$$

The equation 6 is linear, so the amplitudes of the odd modes P_1 and P_3 can be determinate without ambiguity. In the equation 5, the only unknown is the amplitude of the even mode P_2 but the sign cannot be measured from a single image. In our algorithm we implemented a trial-and-error approach to deal with this sign ambiguity.

Once measured, the 9 LWE modes correction is applied in the AO loop via a modification of the reference slopes. As described in the previous section, the petal modes in the phase space contain phase discontinuities that are badly seen by the SH. In order to smooth the discontinuities, we project the LWE petal modes into the KL basis to obtain the matrices $\underline{\mathbf{PTT2K}}$ and $\underline{\mathbf{PP2K}}$. Then we use the interaction matrix $\underline{\mathbf{K2S}}$ to obtain $\underline{\mathbf{PTT2S}}$ and $\underline{\mathbf{PP2S}}$, the best expression of the LWE modes in the slopes space:

$$\underline{\mathbf{PTT2S}} = \underline{\mathbf{K2S}} \cdot \underline{\mathbf{PTT2K}}, \tag{7}$$

$$\underline{\mathbf{PP2S}} = \underline{\mathbf{K2S}} \cdot \underline{\mathbf{PP2K}}. \tag{8}$$

Finally, using the PTT amplitudes measured with the SH and the PP amplitudes measured at the focal plane we can modify the reference slopes during the AO loop operation and correct for the 9 LWE modes (Fig. 14).

Regarding the temporal aspects, it is necessary to decouple the PTT correction to the atmosphere correction by the AO loop. If we do not, the PTT control will come into conflict with the atmosphere correction and disturb the nominal AO loop operation. To avoid this, we apply the LWE PTT correction with a low gain at 0.005 when the full KL atmosphere correction is applied with a gain of 0.3. This way the PTT algorithm take 170 ms to converge, that is enough to control for the LWE that evolves on a timescale of a few seconds. On the petal-piston side, the DTTS on SPHERE and the acquisition camera on GRAVITY can provide H-band images at a frequency around 1 Hz. It means that the PP correction algorithm can converge on a timescale of 10 s. At this timescale there is no risk to disturb the atmosphere correction but it is also too slow to correct for the fast LWE evolution on a timescale of 1∼2 sec. Still, it can correct for the quasi-static component of the LWE. The low measurement frequency of focal plane analysis justifies the use of the faster SH to measure as much as possible LWE modes.

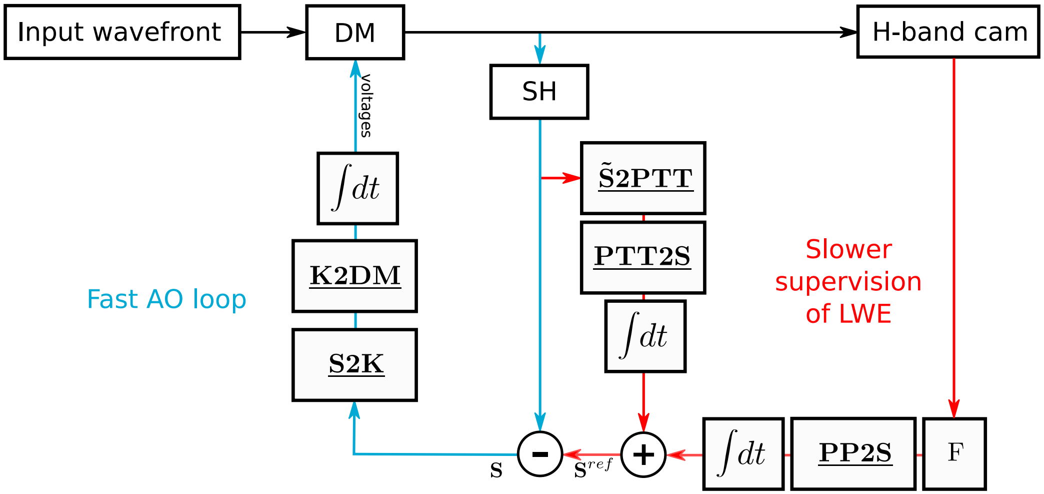

Figure 14: Schematic for the LWE mitigation algorithm. Cyan: main AO loop. Red: loop for LWE control. $\int dt$ are integrators. F is the operation that extracts the three PP modes amplitudes from the H-band images. $\tilde{\mathbf{S}}$ refers to the slopes selected inside the quadrants for PTT measurement (Fig. 13).

We tested our mitigation strategy in simulations. We used the SPHERE-like end-to-end AO simulation described at the previous section. The only difference is that we do not use the DTTS as a tip-tilt sensor but has a PP sensor (as described previously). We simulate LWE with two static phase patterns containing PP and PTT as perturbations. The LWE#1 induce post-AO residuals that correspond to what has been observed on SPHERE (Fig. 9a). The post-AO residuals contain 173 nm rms and 650 nm peak-to-valley OPD. The LWE#2 induces stronger PTT in the post-AO residuals. For this pattern the residuals are of 276 nm rms and 1350 nm peak-to-valley OPD. This pattern is meant to test the algorithm limit in the PTT correction. Additionally, we included a simulated atmosphere with Fried parameter $r_0 = 16.8$ cm and coherence time $\tau_0 = 5$ ms (both defined at $\lambda = 500$ nm). Adding an atmosphere permit to check that the SH PTT control and the atmosphere control are well decoupled in the AO loop.

The tests results for the mitigation algorithm are displayed on Fig. 15. For both LWE#1 and LWE#2 perturbations the algorithm converged to weaker PTT modes in a timescale around 150 ms. For LWE#1 the Strehl at H-band before the algorithm correction is 65% and the PTT control algorithm allow for a +16% Strehl recovering. After the algorithm convergence virtually no PTT are visible in the post-AO residuals anymore. If we run the PP control on LWE#1 we recover an additional +4% Strehl. The best fitting of the LWE modes in the 990 KL space (directly projecting the AO residuals from the phase space to the KL space, thus avoiding the measurement stage) reach 88% Strehl. Our correction algorithm reaches 85% Strehl, only 3 points below the best achievable correction. It validates our measurement strategy. For LWE#2 the Strehl before the algorithm correction is 31% and the PTT control recovers +30% Strehl. With the PP control the algorithm reaches 77% Strehl, 9 points below the best achievable correction in the KL space. The residuals after PTT+PP correction contain local vortexes around the spiders that are not captured by our SH-based measurement.

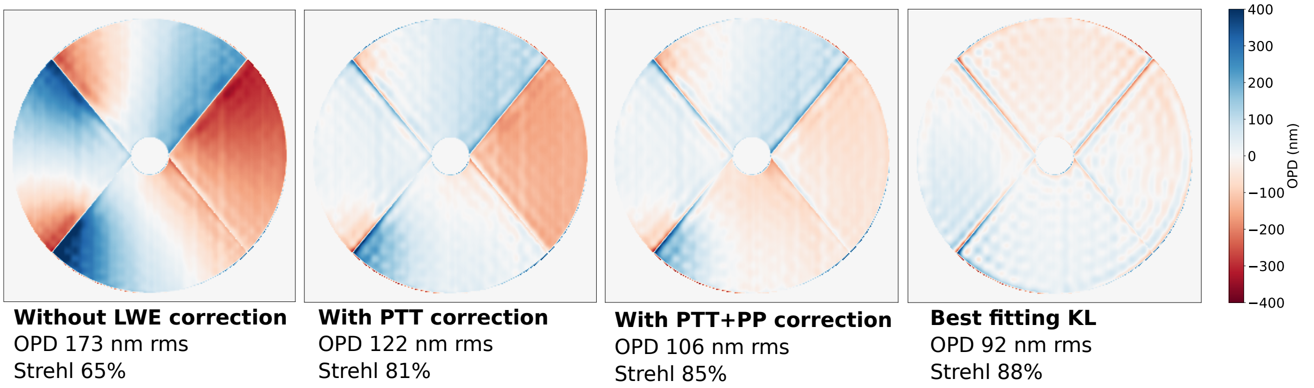

(a) LWE#1

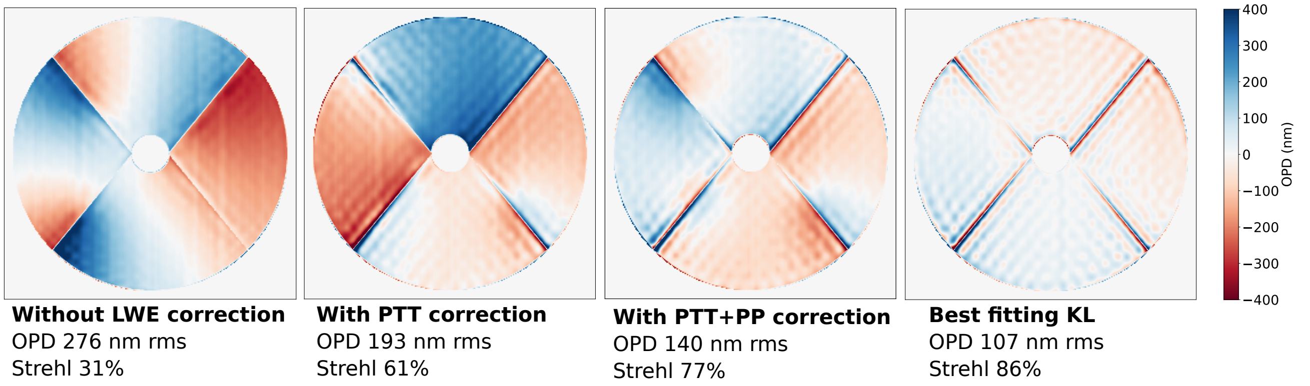

(b) LWE#2

Figure 15: Post AO residuals for (a) LWE#1 and (b) LWE#2 in different configurations. The residual are averaged over 2 seconds to reduce the atmosphere contribution. The Strehl ratios are given at H-band.

5. CONCLUSIONS

Our study shows that the SH is unable to measure obstructed discontinuities. In LWE conditions, these faulty measurements are responsible for uncorrected petal-pistons and petal-tip-tilts in the post-AO residuals. We also show that a local perturbation along the spiders is enough to reproduce the full pupil uncorrected aberrations observed on SPHERE. In this framework, the AO is responsible for most of the wavefront degradation. Then, we predict that on the next generation telescopes like the ELT the LWE will be a petal-piston problem only since with spiders thicker than the SH sub-apertures no petal-tip-tilt can arise in the AO residuals. Finally, we found that 8 out of 11 LWE modes can be corrected with the SH in AO similar to SPHERE's or GRAVITY+. We successfully tested in simulations a mitigation strategy that uses both the SH and a focal plane analysis for the measurement of the LWE modes.

ACKNOWLEDGMENTS

N. P. was supported by the Action Spécifique Haute Résolution Angulaire (ASHRA) of CNRS/INSU co-funded by CNES. The authors acknowledges the support of the French Agence Nationale de la Recherche (ANR), under grant ANR-21-CE31-0017 (project EXOVLTI). The authors would like to thanks Dr. Eric Gendron for pointing us in the direction of curl structures in AO residuals, Dr. Olivier Lai for a very interesting discussion he initiated on LWE mitigation strategies and Dr. Emiel Por for his kind assistance in the adaptation of HCIPy to our specific problem. We also would like to thanks the GRAVITY+ AO (GPAO) consortium for their support and expertise. This research has made use of the following python packages: matplotlib, numpy, hcipy, astropy and scipy.

REFERENCES

[1] Beuzit, J. L., Vigan, A., Mouillet, D., Dohlen, K., Gratton, R., Boccaletti, A., Sauvage, J. F., Schmid, H. M., Langlois, M., Petit, C., Baruffolo, A., Feldt, M., Milli, J., Wahhaj, Z., Abe, L., Anselmi, U., Antichi, J., Barette, R., Baudrand, J., Baudoz, P., Bazzon, A., Bernardi, P., Blanchard, P., Brast, R., Bruno, P., Buey, T., Carbillet, M., Carle, M., Cascone, E., Chapron, F., Charton, J., Chauvin, G., Claudi, R., Costille, A., De Caprio, V., de Boer, J., Delboulbé, A., Desidera, S., Dominik, C., Downing, M., Dupuis, O., Fabron, C., Fantinel, D., Farisato, G., Feautrier, P., Fedrigo, E., Fusco, T., Gigan, P., Ginski, C., Girard, J., Giro, E., Gisler, D., Gluck, L., Gry, C., Henning, T., Hubin, N., Hugot, E., Incorvaia, S., Jaquet, M., Kasper, M., Lagadec, E., Lagrange, A. M., Le Coroller, H., Le Mignant, D., Le Ruyet, B., Lessio, G., Lizon, J. L., Llored, M., Lundin, L., Madec, F., Magnard, Y., Marteaud, M., Martinez, P., Maurel, D., Ménard, F., Mesa, D., Möller-Nilsson, O., Moulin, T., Moutou, C., Origné, A., Parisot, J., Pavlov, A., Perret, D., Pragt, J., Puget, P., Rabou, P., Ramos, J., Reess, J. M., Rigal, F., Rochat, S., Roelfsema, R., Rousset, G., Roux, A., Saisse, M., Salasnich, B., Santambrogio, E., Scuderi, S., Segransan, D., Sevin, A., Siebenmorgen, R., Soenke, C., Stadler, E., Suarez, M., Tiphène, D., Turatto, M., Udry, S., Vakili, F., Waters, L. B. F. M., Weber, L., Wildi, F., Zins, G., and Zurlo, A., "SPHERE: the exoplanet imager for the Very Large Telescope," *A&A* **631**, A155 (Nov. 2019).

[2] Sauvage, J.-F., Fusco, T., Guesalaga, A., Wizinowitch, P., O'Neal, J., N'Diaye, M., Vigan, A., Girard, J., Lesur, G., Mouillet, D., Buezit, J.-L., Kasper, M., Le Louarn, M., Mlli, J., Dohlen, K., Neichel, B., Bourget, P., Heigenauer, P., and Mawet, D., "Low Wind Effect, the main limitation of the SPHERE instrument," in [*Adaptive Optics for Extremely Large Telescopes IV (AO4ELT4)*], E9 (Oct. 2015).

[3] Milli, J., Kasper, M., Bourget, P., Pannetier, C., Mouillet, D., Sauvage, J. F., Reyes, C., Fusco, T., Cantalloube, F., Tristam, K., Wahhaj, Z., Beuzit, J. L., Girard, J. H., Mawet, D., Telle, A., Vigan, A., and N'Diaye, M., "Low wind effect on VLT/SPHERE: impact, mitigation strategy, and results," in [*Adaptive Optics Systems VI*], Close, L. M., Schreiber, L., and Schmidt, D., eds., *Society of Photo-Optical Instrumentation Engineers (SPIE) Conference Series* **10703**, 107032A (July 2018).

[4] N'Diaye, M., Dohlen, K., Caillat, A., Costille, A., Fusco, T., Jolivet, A., Madec, F., Mugnier, L., Paul, B., Sauvage, J.-F., Soummer, R., Vigan, A., and Wallace, J. K., "Design optimization and lab demonstration of ZELDA: a Zernike sensor for near-coronagraph quasi-static measurements," in [*Adaptive Optics Systems IV*], Marchetti, E., Close, L. M., and Vran, J.-P., eds., *Society of Photo-Optical Instrumentation Engineers (SPIE) Conference Series* **9148**, 91485H (Aug. 2014).

[5] N'Diaye, M., Vigan, A., Dohlen, K., Sauvage, J. F., Caillat, A., Costille, A., Girard, J. H. V., Beuzit, J. L., Fusco, T., Blanchard, P., Le Merrer, J., Le Mignant, D., Madec, F., Moreaux, G., Mouillet, D., Puget, P., and Zins, G., "Calibration of quasi-static aberrations in exoplanet direct-imaging instruments with a Zernike phase-mask sensor. II. Concept validation with ZELDA on VLT/SPHERE," *A&A* **592**, A79 (Aug. 2016).

[6] Vievard, S., Bos, S., Cassaing, F., Ceau, A., Guyon, O., Jovanovic, N., Keller, C. U., Lozi, J., Martinache, F., Montmerle-Bonnefois, A., Mugnier, L., NDiaye, M., Norris, B., Sahoo, A., Sauvage, J.-F., Snik, F., Wilby, M. J., and Wong, A., "Overview of focal plane wavefront sensors to correct for the Low Wind Effect on SUBARU/SCExAO," *arXiv e-prints* , arXiv:1912.10179 (Dec. 2019).

[7] Wilby, M. J., Keller, C. U., Sauvage, J. F., Dohlen, K., Fusco, T., Mouillet, D., and Beuzit, J. L., "Laboratory verification of Fast & Furious phase diversity: Towards controlling the low wind effect in the SPHERE instrument," *A&A* **615**, A34 (July 2018).

[8] Bos, S. P., Vievard, S., Wilby, M. J., Snik, F., Lozi, J., Guyon, O., Norris, B. R. M., Jovanovic, N., Martinache, F., Sauvage, J. F., and Keller, C. U., "On-sky verification of Fast and Furious focal-plane wavefront sensing: Moving forward toward controlling the island effect at Subaru/SCExAO," *A&A* **639**, A52 (July 2020).

[9] Por, E. H., Haffert, S. Y., Radhakrishnan, V. M., Doelman, D. S., van Kooten, M., and Bos, S. P., "High Contrast Imaging for Python (HCIPy): an open-source adaptive optics and coronagraph simulator," in [*Adaptive Optics Systems VI*], Close, L. M., Schreiber, L., and Schmidt, D., eds., *Society of Photo-Optical Instrumentation Engineers (SPIE) Conference Series* **10703**, 1070342 (July 2018).

[10] Baudoz, P., Dorn, R. J., Lizon, J.-L., Fusco, T., Dohlen, K., Charton, J., Beuzit, J.-L., Puget, P., Mouillet, D., Felt, M., Wildi, F., Barufolo, A., Kasper, M., and Hubin, N., "The differential tip-tilt sensor of SPHERE," in [*Ground-based and Airborne Instrumentation for Astronomy III*], McLean, I. S., Ramsay, S. K., and Takami, H., eds., *Society of Photo-Optical Instrumentation Engineers (SPIE) Conference Series* **7735**, 77355B (July 2010).

[11] Sauvage, J.-F., Fusco, T., Lamb, M., Girard, J., Brinkmann, M., Guesalaga, A., Wizinowich, P., O'Neal, J., N'Diaye, M., Vigan, A., Mouillet, D., Beuzit, J.-L., Kasper, M., Le Louarn, M., Milli, J., Dohlen, K., Neichel, B., Bourget, P., Haguenauer, P., and Mawet, D., "Tackling down the low wind effect on SPHERE instrument," in [*Adaptive Optics Systems V*], Marchetti, E., Close, L. M., and Véran, J.-P., eds., *Society of Photo-Optical Instrumentation Engineers (SPIE) Conference Series* **9909**, 990916 (July 2016).

[12] N'Diaye, M., Martinache, F., Jovanovic, N., Lozi, J., Guyon, O., Norris, B., Ceau, A., and Mary, D., "Calibration of the island effect: Experimental validation of closed-loop focal plane wavefront control on Subaru/SCExAO," *A&A* **610**, A18 (Feb. 2018).

[13] Korkiakoski, V., Keller, C. U., Doelman, N., Kenworthy, M., Otten, G., and Verhaegen, M., "Fast & Furious focal-plane wavefront sensing," *Applied Optics* **53**, 4565 (July 2014).